RESEARCH ARTICLE

Preparation and Characterization of 3D Printed Porous 45S5 Bioglass Bioceramic for Bone Tissue Engineering Application

Zhihong Dong[1], Jiabao Gong[1], Haowei Zhang[3], Yanting Ni[1], Lijia Cheng[2], Qiaoyu Song[1], Lu Tang[2], Fei Xing[4], Ming Liu[4]*, Changchun Zhou[5]

[1]School of Mechanical Engineering, Chengdu University, Chengdu, 610106, China
[2]Department of Stomatology, The Affiliated Hospital of Chengdu University, Chengdu, 610081, China
[3]College of Electronics and Information Engineering, Sichuan University, Chengdu 610065, China
[4]Department of Orthopedics, West China Hospital, Sichuan University, Chengdu 610041, China
[5]National Engineering Research Center for Biomaterials and College of Biomedical Engineering, Sichuan University, Chengdu 610064, China

Abstract: Three-dimensional (3D) printing technology provides advanced technical support for designing personalized bone tissue engineering scaffold. In this study, two porous diffusing models, namely, average and layered perforated cylindrical scaffolds, were designed for bone tissue engineering scaffold. The designed models were fabricated by liquid crystal display mask stereolithography printing. Structural design and finite element mechanical analysis were conducted. 45S5 bioglass was selected as the raw material for preparing the printing inks for bone tissue engineering scaffolds. By adjusting the viscosity and temperature of the slurry, the maximum proportion of 45S5 bioglass (40 wt%) was added into the photosensitive resin for preparing 3D printing slurry. Our results indicated that an optimized sintering condition includes the debinding rate (0.5°C/min), and temperature raising rate (5°C/min) and sintering temperature (1100°C) were proposed to sinter 45S5 bioceramic scaffolds. The amorphous 45S5 bioglass showed good crystallization after sintering, and the scaffold porous structure showed good integrity. Micropores were observed in the struts which interconnected with each other. Moreover, the porosities were tested as 57% and 45% with a uniform pore distribution. The shrinkage rate was about 10% during sintering process due to binder burning and crystallization shrinkage. The compressive strength of the sintered scaffold was 0.71 ± 0.048 MPa and 2.13 ± 0.054 MPa, respectively, which are consistent with the finite element mechanical analysis simulation results. In conclusion, the layered perforated 45S5 bioglass scaffold shows good mechanical properties and porosity, indicating that it could be a promising candidate for bone tissue engineering.

Keywords: 3D printing; LCD stereolithography; 45S5 Bioglass; Bone tissue engineering

***Correspondence to:** Ming Liu, Department of Orthopedics, West China Hospital, Sichuan University, Chengdu 610041, China Department of Orthopedics, West China Hospital, Sichuan University, Chengdu 610041, China; liuming15@qq.com

Received: April 24, 2022; **Accepted:** May 31, 2022; **Published Online:** September 1, 2022

(This article belongs to the *Special Issue: Additive Manufacturing of Functional Biomaterials*)

Citation: Dong Z, Gong J, Zhang H, *et al*., 2022. Preparation and Characterization of 3D Printed Porous 45S5 Bioglass Bioceramic for Bone Tissue Engineering Application, *Int J Bioprint,* 8(4): 613. http://doi.org/10.18063/ijb.v8i4.613

1. Introduction

Three-dimensional (3D) printing technology shows a great potential for biomedical applications[1,2], such as bone tissue engineering[3,4], especially in customized implants and bone scaffolds[5-7]. Although bone has a good self-regeneration ability, large bone defects cannot repair by themselves; in this case, the reconstruction of bone scaffolds is necessary to help with the bone repair and rebuilding. Artificial bone scaffold has three basic characteristics: porosity, pore

interconnection, and mechanical properties[8,9]. In recent years, various artificial bone scaffold materials, such as metal[10], bioceramic[11,12], polymer[13], and other kinds of composites[14,15], have undergone rapid development and been successfully used as bone substitutes. However, the precise size of the bone scaffolds requires specific design. Based on these issues, 3D printed scaffolds have been extensively studied for customized bone tissue repair, which employs a combination of materials from computation 3D models and layer-by-layer fabrication. Thus, many different structures have been designed[16,17] and various fabrication techniques have been employed to produce porous scaffolds through 3D printing technology, such as laser-based[18], extrusion-based[19,20] and inkjet printing[21], as well as lithography rapid prototyping[22]. Lithography-based 3D printing such as digital light processing (DLP) and liquid crystal display (LCD) may fabricate the bioglass or ceramic scaffolds using photopolymer and ceramics composite, and further sintering is needed to obtain the scaffolds[23,24]. Hence, it is necessary to focus on the shape and topology optimization to reduce cost in the design of bone scaffold with good porosity and mechanical properties[25].

Various biomedical ceramic materials used as the bone repair scaffolds were widely studied, including calcium phosphate-based[26,27] and calcium silicate-based bioceramics[28,29]. Calcium silicon bioceramics have been extensively investigated in bone repair due to their good biocompatibility and degradability. For example, 45S5 bioglass was used to prepare porous scaffold in various biomedical fields[30,31]. However, because of the brittleness of 45S5, conventional fabrication techniques are unsuccessful in fabricating final products with complex shapes. As a result, the use of bioglass was mostly limited to powder or composite scaffold[32,33]. To achieve a superior scaffold after sintering, photopolymerization-based LCD mask stereolithography 3D printing technique was proposed[34]. Although the accuracy of LCD printing technique is less than that of DLP, LCD equipment is cheap, and its operation is much easier. For 3D printing of ceramic, further sintering is usually needed, so the printing accuracy can be comprehensively considered during sintering even if LCD is less accurate than DLP. Furthermore, 3D printed bioceramic scaffold for bone tissue does not need high precision (printing accuracy <50 um). In view of this, the specimens were fabricated through LCD in this study. LCD has the advantages of fast printing speed, good molding, and good printability with higher concentration ceramic powders in the inks. The porosity precision is controllable by designing the sample structure. However, a higher proportion of ceramic suspension would increase the viscosity and fluidity, hindering its applications[20]. Hence, it is very important to adjust the process parameters.

In this study, a low-cost LCD strategy was used to print porous 45S5 bioglass bone scaffolds. Different aspects from design to printing process, including percentage content of dispersant, reheated temperature, and mixed ratio of 45S5 suspension, were studied. Different structures and porosities that may affect the compressive strength of final scaffolds were investigated. X-ray crystallography (XRD), scanning electron microscopy (SEM), micro-computed tomography (micro-CT), and mechanical compression test were used for analyzing the sintered scaffolds. Our results demonstrated that the proposed 45S5 scaffolds fabricated by LCD mask stereolithography technology are well-designed in terms of composition, morphology, porosity, and mechanical properties. This scaffold could be a promising substitute in bone tissue repair.

2. Materials and methods

2.1. Design of 3D scaffolds and finite analysis

To build 3D scaffold models, Solidworks 2020 software (Solid Works Corp, SUA) was used. Two cylindrical scaffold models with the size of Φ 15 × 15 mm were designed, but the porosity was different: one was average perforated cylindrical scaffold with 53% porosity, and the other was layered perforated cylindrical scaffold with 43% porosity. Images of scaffold design models are shown in **Figure 1A and B**.

The equivalent stress and total deformation of the model under axial load were evaluated by finite element analysis software (NASDAQ: ANSS). Under linear

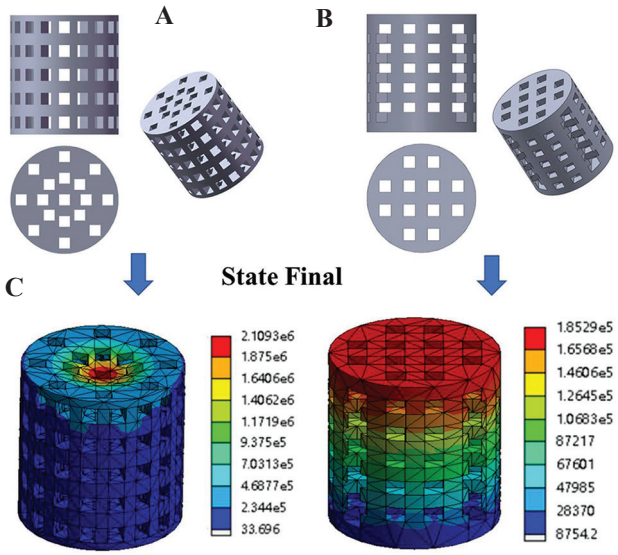

Figure 1. (A) Average perforated cylindrical scaffold model. (B) Layered perforated cylindrical scaffold model. (C) Corresponding equivalent stress by finite element analysis simulation.

and static conditions, the load was gradually applied to the limit and the compressive strength was evaluated. Maximum equivalent stress was obtained under the same process parameters, 2.11 MPa and 0.19 MPa corresponding diagrams are shown in **Figure 1C**. The stimulated result indicated that the mechanical properties of scaffold B were superior to that of scaffold A.

2.2. LCD mask stereolithography printing and slurry preparation

An image of LCD mask stereolithography printer (Anycubic Photon Mono-China) is shown in **Figure 2A**. The overall size was 222 mm (L) × 227 mm (W) × 383 mm (H), the printing platform size was 130 mm (L) × 80 mm (W) × 165 mm (H), the resolution was 2560 × 1620 pixels, and 2K LCD screen was used. The designed scaffold models were put into Photo Workshop software in STL format and then the printing parameters were adjusted. A schematic diagram about its principle is shown in **Figure 2B**. The ultraviolet (UV) light was emitted by the LCD array and homogenized by the lens array. When the LCD screen displayed the mask, the inner liquid crystal of the mask region rearranged to allow the UV light to pass through. The designed scaffold models were output in STL format after modeling. In the printing process, a layer thickness of 0.06 mm, 4-s exposure time, a Z-axis speed of 3 mm/s, and filling rates at 100% were set.

The slurry consisted of 45S5 bioglass powder with a particle size range of 5 – 30 μm (3M, USA), photosensitive resin (Esun materials, China), and oleic acid dispersant (Sinopharm, China); the maximum

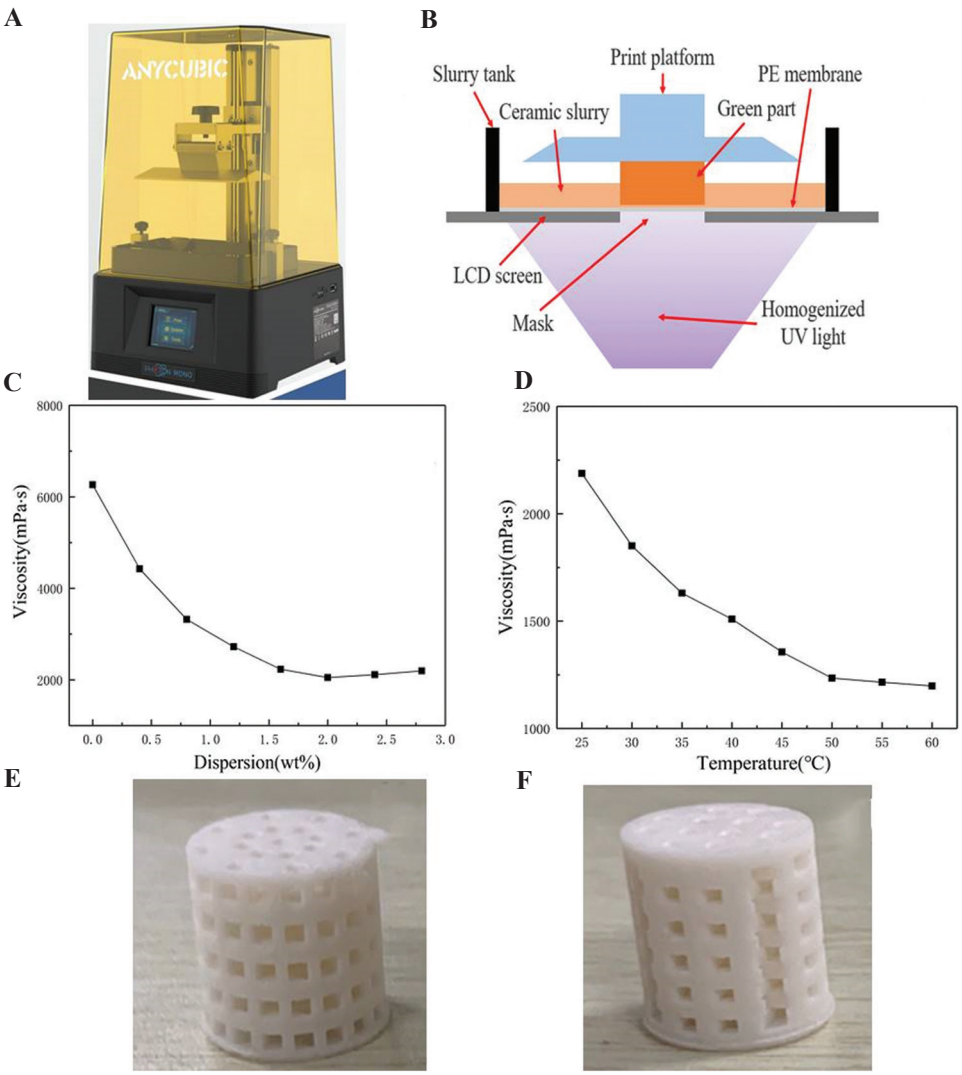

Figure 2. (A) LCD mask stereolithography printer, and (B) a schematic diagram depicting its principle. The viscosity changes of composite slurry under different conditions: the oleic acid dispersion (C) and the reheated temperature (D). (E) A printed perforated cylindrical scaffold. (F) A layered perforated cylindrical scaffold.

percentage content of bioglass powder was 40 wt%. Specific processes were followed. Bioglass and resin in a ratio of 40:60 were mixed and stirred under planetary ball mill for 8 h to obtain the compound solution. The ball mill rotation speed was 300 rom. Then, different proportion of oleic acid dispersant was added, stirring was continued mechanically for 10 min, and the viscosity was adjusted in order to process molding. The composite slurry was put into a water bath, heated to reduce its viscosity, and then put into the LCD mask stereolithography printer to fabricate the scaffolds.

2.3. Debinding sinter and sample characterization

The printed green scaffolds were put into muffle furnace for debinding sintering with different heating rates of 0.5°C/min, 1°C/min, 2°C/min. When the temperature reached at 100°C, 200°C and 300°C, the temperatures were hold for 60 min, while the temperature reached at 400°C and 500°C, the temperatures were hold for 120 min, respectively. After debinding, sintering rate was 5°C/min. The maximum sintering temperatures were 1000°C, 1100°C, and 1200°C, and the temperatures were sustained for 120 min. Finally, the samples were cooled in the furnace at room temperature.

The microstructure formed during 3D printing, debinding, and sintering process was recorded using a Leica camera (Germany). The thermal stability of sintered samples was evaluated by thermogravimetric (TG) and differential thermogravimetric (DTG) analyses so as to measure the change temperature of debinding process. Samples were heated from 30°C to 700°C under nitrogen atmosphere (flow of 25 mL/min) at a heating rate of 10°C/min. Phase structure of pre- and post-sintering scaffolds was determined by XRD (MAXima, Shimadzu Co., Japan) at 40 kV, 30 mA with monochromatic Cu-Kα radiation, typically with scan speed of 0.5°/min and sampling pitch of 0.03° in a 2θ scale region of 10 – 65°. Morphology of 3D printed scaffolds was observed using SEM (JSE-6700F, JEOL, Japan). Sintered 3D scaffolds were scanned and reconstructed in three dimensions by micro-CT (Quantum GX, USA). The true porosity of the sintered scaffolds was analyzed and calculated using 3D modeling software. The mechanical compression of the printed scaffolds was tested by an electronic universal testing machine (INSTRON, USA). The standard cylinder (Φ 15 × 15 mm) was stressed at a speed of 0.1 mm/min. The maximum compression stress described in this study referred to the compression stress when the specimen broke during the compression test. All samples were tested and the average values are expressed as mean ± standard deviation. The results were analyzed using two-way analysis of variance. A $P < 0.05$ was considered statistically significant.

3. Results and discussion

3.1. Suspension, debinding, and sintering of samples

To meet the formability of the scaffold, the viscosity of slurry was adjusted to optimum proportions of 2 wt% oleic acid dispersant at 50°C (**Figure 2C and D**). The 45S5 bioglass was uniformly dispersed in the resin solution; therefore, two ideal scaffolds were obtained (**Figure 2E and F**). The use of good dispersant was beneficial to reduce the viscosity of the suspension, thereby achieving good homogeneity and mobility. The casting of the suspensions allowed for suitable viscosity at a proper temperature in the LCD mask stereolithography process[35,36].

The debinding behavior of green composite scaffolds was evaluated by TG and DTG analyses (**Figure 3A**). The results showed that the debinding temperature occurred between 200°C and 550°C. When the temperature changed in the range of 100 – 300°C, the reduction of weight loss rate was not obvious, which indicates an endothermic effect mainly caused by the evaporation of free water and some small molecules with low melting point[37]. When the temperature continued to rise up to about 383°C, the DTG curve showed an obvious weight loss peak, and the weight loss rate of green scaffolds reached the maximum and the pyrolysis rate of photosensitive resin reached the highest point (0.1%/°C). When the temperature reached above 550°C, the weight of samples was basically stable. These results indicated that the organic resin of scaffold had been completely removed at 550°C. According to thermal analysis, when debinding, it was necessary to keep the temperatures of the samples at 300°C, 383°C and 550°C to obtain complete scaffold structure. Otherwise, the scaffold would collapse in the debinding process.

Based on the TG and DTG analyses, the heating rates of debinding were set to 2°C/min, 1°C/min, and 0.5°C/min and the temperature was sustained at every temperature gradient (**Figure 3B**). The results indicated that the heating rate was very high (2°C/min, 1°C/min), leading to the collapse of scaffolds, and when the heating rate was slowed down to 0.5°C/min, scaffolds were completely debinded and their integrity were maintained by Van der Waals force (**Figure 3C**).

The results at three different sintering temperatures indicated that: (i) the scaffold had completely collapsed at 1000°C; (ii) when the sintering temperature was 1100°C, the scaffold experienced almost no collapse and showed good pore structure; and (iii) while at 1200°C, part of the scaffold deformed and shrunk greatly (**Figure 3D**). When the sintering temperature was too low, the growth of ceramic grains was not sufficient, leading to weak bonding among

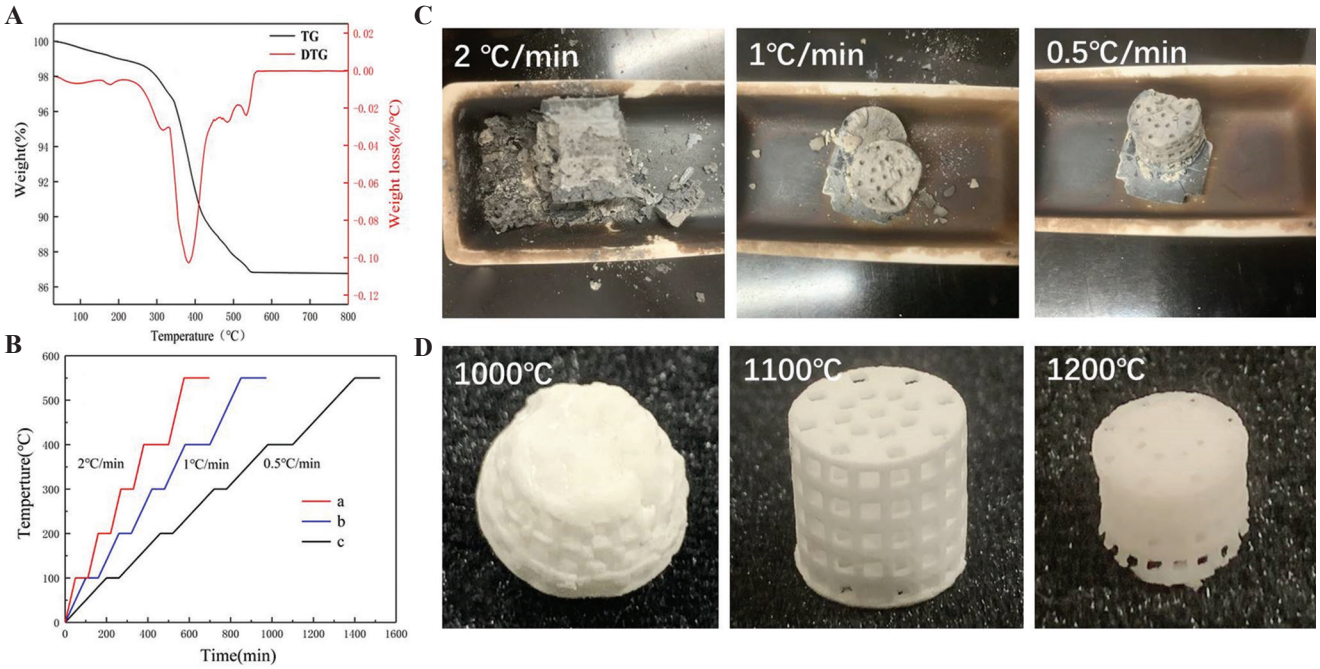

Figure 3. The sintering properties and the sintered scaffolds. (A) TG and DTG analyses. (B) Different sintering curve and its comparison of heating rate of debinding and sintering temperature. (C and D) The obtained scaffolds sintered by different curve and their corresponding morphology.

the grains. When the sintering temperature was too high, most of the grains grew abnormally, leading to excessive shrinkage of the scaffold. This shrinkage exceeded that of the normally grown grains, which severely deformed and even broke the scaffolds. In view of this, 1100°C was set as the optimal sintering temperature. This was also consistent with the findings from other studies that 45S5 bioactive glass powder above 1000°C must be sintered quickly and effectively so that the particles grow densely to produce sufficient mechanical strength[38,39].

3.2. Components and structure of samples after sintering

Components of sintered samples were analyzed by XRD, as shown in **Figure 4**. 45S5 bioglass powder was an amorphous structure (**Figure 4: blue curve**). After sintering, organic components were completely decomposed, and some new peaks appeared as a result of crystallization (**Figure 4: red curve**). One peak closely matched the standard JCPDF card 77-2189, confirming that the major crystalline phase was $Na_6Ca_3Si_6O_{18}$, while other minor peaks which were the second phase represented $Na_2Ca_4(PO_4)_2Si_2O_4$, which matched the JCPDF card 32-1053. All these results were in accordance with the previous reports[40].

The sintering scaffold samples were observed using SEM and the results are shown in **Figure 5**. The structure

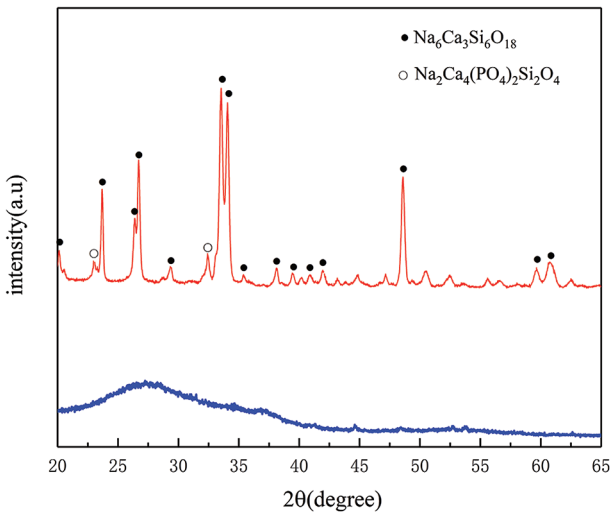

Figure 4. XRD patterns of 45S5 bioglass powders (blue curve), 3D printed scaffold after sintering at 1100°C for 2 h (red curve). The peaks of the $Na_6Ca_3Si_6O_{18}$ phase and $Na_2Ca_4(PO_4)_2Si_2O_4$ phase were marked by ● and ○, respectively.

of the two scaffolds had good integrity, and uniform pores were about 600 μm in diameter. Macropores were interconnected with micropores, with the size of 5 – 10 μm. Rough surface structure may supply for the cell adhesion and proliferation, and interconnected pores may supply for cell nutrient transportation and bone bioconductivity[41,42]. A low concentration of green

scaffolds (40 wt%) produced large shrinkage after sintering. Moreover, based on the scaffold structure design, the porosity of average perforated cylindrical scaffold (**Figure 5A**) was higher than that of layered

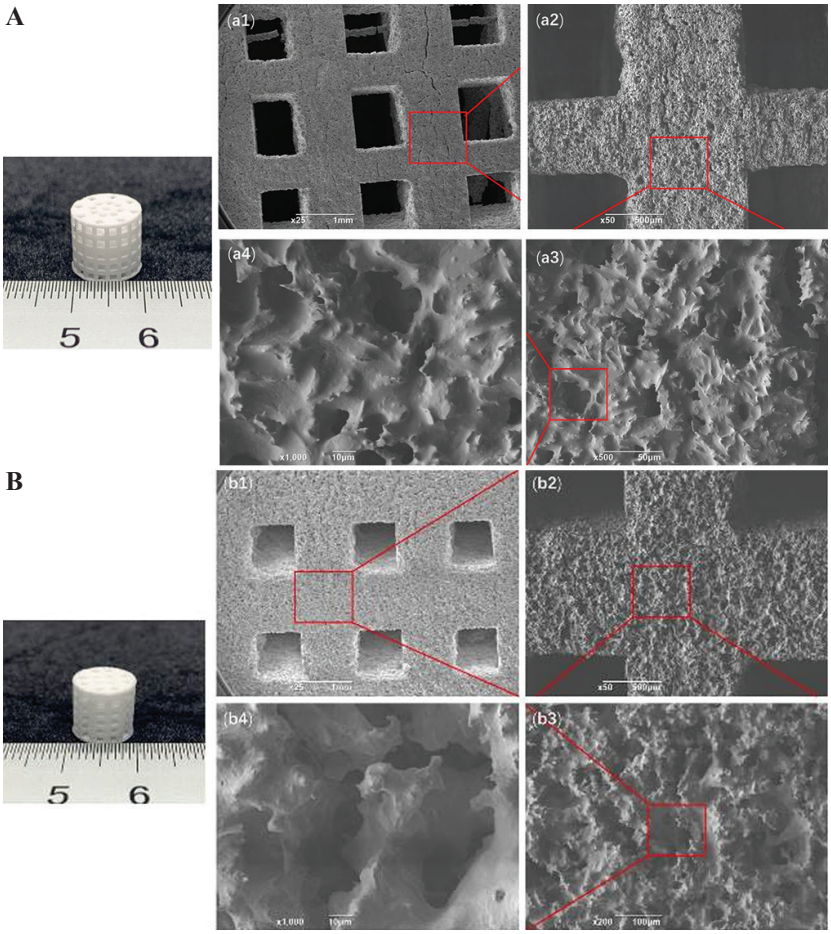

Figure 5. Images of average perforated cylindrical scaffold. (A) A printed layered perforated cylindrical scaffold. (B) A sintered scaffold. (A and B) show images of the overall structures of the scaffolds. (a1 – a2) and (b1 – b2) show the struts of the 3D printed scaffolds, and (a3 – a4) and (b3 – b4) are the SEM images of their microstructures.

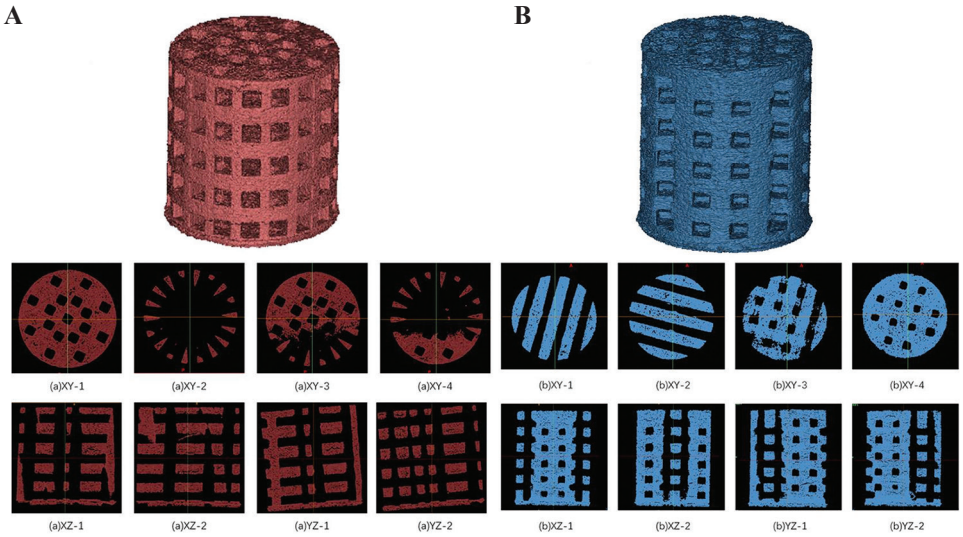

Figure 6. CT reconstruction of scaffold 3D images. (A) Average perforated cylindrical scaffold. (B) Layered perforated cylindrical scaffold.

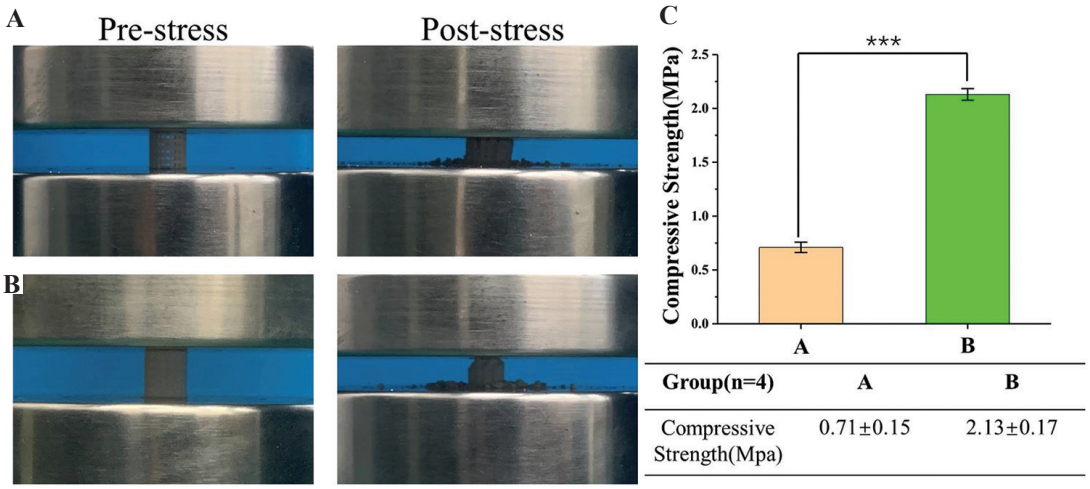

Group(n=4)	A	B
Compressive Strength(Mpa)	0.71±0.15	2.13±0.17

Figure 7. Mechanical test of 3D printed samples. (A and B) Average and layered perforated cylindrical scaffolds before pressure test and after pressure test. (C) The mechanical properties test results. ***$P < 0.001$.

perforated cylindrical scaffold (**Figure 5B**). By applying Mimics 3D and micro-CT reconstruction and calculation (**Figure 6**), we determined that the macroporosities of average perforated cylindrical scaffold (A) and layered perforated cylindrical scaffold (B) after sintering were 57% and 45%, respectively. The scaffolds showed a complete and regular structure and good pore connectivity in XY section. This modern processing technology allows for the fabrication of scaffold with better structure for bone tissue regeneration as well as diagnosis and treatment[43,44].

3.3. Mechanical properties test

Mechanical tests were conducted on the two kinds of scaffolds after sintering until the scaffold ruptured after compression (**Figure 7A and 7B**). The compressive strength of average perforated cylindrical scaffolds was 0.71 ± 0.048 MPa and that of layered perforated cylindrical scaffolds was 2.13 ± 0.05 MPa (**Figure 7C**), which was close to the standard for a porous ceramic bone implant (2.40 MPa) (ISO 13779). Mechanical performance decreased with the porosity of scaffold A increased, while scaffold B improved the porosity and had good mechanical performance. These results indicated that scaffold B could meet the requirements of natural human cancellous bone (1 – 12 MPa)[45].

4. Conclusion

Using LCD mask stereolithography technique, 40 wt% porous bioglass scaffold was successfully fabricated for bone tissue engineering scaffolds. Mechanical properties test results indicated that the compressive strength was about 2.13 ± 0.054 MPa, which was within the lower limit of the compressive strength of cancellous bone. Suspension slurry was optimized for 2 wt% oleic acid dispersant at 50°C, a debinding rate of 0.5°C/min, and a sintering temperature at 1100°C hold for 2 h, which guarantee the production of a good sintered specimen. The sintered specimen has multiple levels of macropores and capillary micropore structures. These results indicated that the LCD mask stereolithography technique can be used to design and fabricate porous 45S5 bioglass scaffolds. As a biomaterial with excellent biological functions, this customized porous 45S5 bioglass scaffold is expected to be a good substitute for use in bone tissue repair.

Funding

The research was supported by the Key Project of Sichuan Medical Association (Q17002), Chengdu Municipal Technological Innovation R&D Project (2021-YF05-01871-SN), Project of Chengdu Municipal Health Commission (2021059). The 1·3·5 Project for Disciplines of Excellence, West China Hospital, Sichuan University (ZYGD21001, ZYJC21026, ZYJC21077), Project of Chengdu Science and Technology Bureau (2021-YF05-01619-SN, 2021-RC05-00022-CG), and Sichuan University Panzhihua Science and Technology Cooperation Project (2021CDPZH-4).

Conflict of interest

The authors declare no conflict of interest regarding the publication of this paper.

Author contributions

Conceptualization: Zhihong Dong, Ming Liu, Changchun Zhou

Investigation: Jiabao Gong, Haowei Zhang, Yanting Ni, Lijia Cheng
Formal analysis: Qiaoyu Song, Lu Tang, Fei Xing
Writing – original draft: Zhihong Dong, Changchun Zhou
Writing – review and editing: Ming Liu, Changchun Zhou

References

1. Jakus AE, Rutz AL, Shah RN, 2016, Advancing the Field of 3D Biomaterial Printing. *Biomed Mater*, 11:014102. https://doi.org/10.1088/1748-6041/11/1/014102
2. Michael L, Sarah S, Shayne H, *et al*., 2022, 3D Printing of Ceramic Biomaterials. *Eng Regen*, 3:41–52. https://doi.org/10.1016/j.engreg.2022.01.006
3. Varma MV, Kandasubramanian B, Ibrahim SM, 2020, 3D Printed Scaffolds for Biomedical Applications. *Mater Chem Phys*, 255:123642. https://doi.org/10.1016/j.matchemphys.2020.123642
4. Dabbagh SR, Sarabi MR, Rahbarghazi R, *et al*., 2021, 3D-printed Microneedles in Biomedical Applications. *iScience*, 24:102012. https://doi.org/10.1016/j.isci.2020.102012
5. Sun H, Zhang C, Zhang B, *et al*., 2022, 3D Printed Calcium Phosphate Scaffolds with Controlled Release of Osteogenic Drugs for Bone Regeneration. *Chem Eng J*, 427:130961. https://doi.org/10.1016/j.cej.2021.130961
6. Liu X, Chen M, Luo J, *et al*., 2021, Immunopolarization-regulated 3D Printed-electrospun Fibrous Scaffolds for Bone Regeneration. *Biomaterials*, 276:121037. https://doi.org/10.1016/j.biomaterials.2021.121037
7. Lin K, Sheikh R, Romanazzo S, *et al*., 2019, 3D Printing of Bioceramic Scaffolds-Barriers to the Clinical Translation: From Promise to Reality, and Future Perspectives. *Materials*, 12:2660–80. https://doi.org/10.3390/ma12172660
8. Shi C, Hou X, Zhao D, *et al*., 2022, Preparation of the Bioglass/Chitosan-alginate Composite Scaffolds with High Bioactivity and Mechanical Properties as Bone Graft Materials. *J Mech Behav Biome Mater*, 126:105062. https://doi.org/10.1016/j.jmbbm.2021.105062
9. Faour O, Dimitriou R, Cousins CA, *et al*., 2011, The Use of Bone Graft Substitutes in Large Cancellous Voids: Any Specific Needs? *Injury*, 42:S87–90. https://doi.org/10.1016/j.injury.2011.06.020
10. Liang H, Zhao D, Feng X, *et al*., 2020, 3D-printed Porous Titanium Scaffolds Incorporating Niobium for High Bone Regeneration Capacity. *Mater Des*, 194:108890. https://doi.org/10.1016/j.matdes.2020.108890
11. Ma H, Feng C, Chang J, *et al*., 2018, 3D-printed Bioceramic Scaffolds: From Bone Tissue Engineering to Tumor Therapy. *Acta Biomater*, 79:37–59. https://doi.org/10.1016/j.actbio.2018.08.026
12. Gao C, Yao M, Shuai C, *et al*., 2020, Advances in Bioceramics for Bone Implant Applications. *Biodes Manuf*, 3:307–30. https://doi.org/10.1007/s42242-020-00087-3
13. Amiryaghoubi N, Fathi M, Barzegari A, *et al*., 2021, Recent Advances in Polymeric Scaffolds Containing Carbon Nanotube and Graphene Oxide for Cartilage and Bone Regeneration. *Mater Today Commun*, 26:102097. https://doi.org/10.1016/j.mtcomm.2021.102097
14. Abdal-Hay A, Sheikh FA, Shmroukh AN, *et al*., 2021, Immobilization of Bioactive Glass Ceramics @ 2D and 3D Polyamide Polymer Substrates for Bone Tissue Regeneration. *Mater Des*, 210:110094. https://doi.org/10.1016/j.matdes.2021.110094
15. Zerankeshi MM, Bakhshi R, Alizadeh R, 2022, Polymer/Metal Composite 3D Porous Bone Tissue Engineering Scaffolds Fabricated by Additive Manufacturing Techniques: A Review. *Bioprinting*, 25:e00191. https://doi.org/10.1016/j.bprint.2022.e00191
16. Mirkhalaf M, Wang X, Entezari A, *et al*., 2021, Redefining Architectural Effects in 3D Printed Scaffolds through Rational Design for Optimal Bone Tissue Regeneration. *Appl Mater Today*, 25:101168. https://doi.org/10.1016/j.apmt.2021.101168
17. Roque R, Barbosa GF, Guastaldi AC, 2021, Design and 3D Bioprinting of Interconnected Porous Scaffolds for Bone Regeneration. An Additive Manufacturing Approach. *J Manuf Processes*, 64:655–63. https://doi.org/10.1016/j.jmapro.2021.01.057
18. Schiele NR, Corr DT, Huang Y, *et al*., 2010, Laser-based Direct-write Techniques for Cell Printing. *Biofabrication*, 2:032001. https://doi.org/10.1088/1758-5082/2/3/032001
19. Beheshtizadeh N, Azami M, Abbasi H, *et al*., 2021, Applying Extrusion-based 3D Printing Technique Accelerates Fabricating Complex Biphasic Calcium Phosphate-based Scaffolds for Bone Tissue Regeneration. *J Adv Res*, In Press. https://doi.org/10.1016/j.jare.2021.12.012
20. Kang JH, Jang KJ, Sakthiabirami K, *et al*., 2020, Mechanical Properties and Optical Evaluation of Scaffolds Produced from 45S5 Bioactive Glass Suspensions Via Stereolithography. *Ceram Int*, 46:2481–8. https://doi.org/10.1016/j.ceramint.2019.09.242
21. Kumar P, Ebbens S, Zhao X, 2021, Inkjet Printing of

Mammalian Cells Theory and Applications. *Bioprinting*, 23:e00157.
https://doi.org/10.1016/j.bprint.2021.e00157

22. Melchels FP, Feijen J, Grijpma DW, 2010, A Review on Stereolithography and its Applications in Biomedical Engineering. *Biomaterials*, 31:6121–30.
https://doi.org/10.1016/j.biomaterials.2010.04.050

23. Tesavibul P, Felzmann R, Gruber S, *et al*., 2012, Processing of 45S5 Bioglass® by Lithography-based Additive Manufacturing. *Mater Lett*, 74:81–4.
https://doi.org/10.1016/j.matlet.2012.01.019

24. Li X, Yuan Y, Liu L, *et al*., 2020, 3D Printing of Hydroxyapatite/Tricalcium Phosphate Scaffold with Hierarchical Porous Structure for Bone Regeneration. *Biodes Manuf*, 3:15–29.
https://doi.org/10.1007/s42242-019-00056-5

25. Wu X, Xu C, Zhang Z, 2021, Preparation and Optimization of Si_3N_4 Ceramic Slurry for Low-cost LCD Mask Stereolithography. *Ceram Int*, 47:9400–8.
https://doi.org/10.1016/j.ceramint.2020.12.072

26. Irbe Z, Loca D, 2021, Soluble Phosphate Salts as Setting Aids for Premixed Calcium Phosphate Bone Cement Pastes. *Ceram Int*, 47:24012–9.
https://doi.org/10.1016/j.ceramint.2021.05.110

27. Carino A, Ludwig C, Cervellino A, *et al*., 2018, Formation and Transformation of Calcium Phosphate Phases Under Biologically Relevant Conditions: Experiments and Modelling. *Acta Biomater*, 74:478–88.
https://doi.org/10.1016/j.actbio.2018.05.027

28. Oryan A, Alidadi S, 2018, Reconstruction of Radial Bone Defect in Rat by Calcium Silicate Biomaterials. *Life Sci*, 201:45–53.
https://doi.org/10.1016/j.lfs.2018.03.048

29. Chen L, Deng C, Li J, *et al*., 2019, 3D Printing of a Lithium-Calcium-Silicate Crystal Bioscaffold with Dual Bioactivities for Osteochondral Interface Reconstruction, *Biomaterials*, 196:138–50.
https://doi.org/10.1016/j.biomaterials.2018.04.005

30. Jurczyk MU, Jurczyk K, Miklaszewski A, *et al*., 2011, Nanostructured Titanium-45S5 Bioglass Scaffold Composites for Medical Applications. *Mater Des*, 32:4882–9.
https://doi.org/10.1016/j.matdes.2011.06.005

31. Schmitz SI, Widholz B, Essers C, *et al*., 2020, Superior Biocompatibility and Comparable Osteoinductive Properties: Sodium-reduced Fluoride-containing Bioactive Glass Belonging to the CaO-MgO-SiO_2 System as a Promising Alternative to 45S5 Bioactive Glass. *Bioact Mater*, 5:55–65.
https://doi.org/10.1016/j.bioactmat.2019.12.005

32. Martel A, Armendáriz IO, García AT, *et al*., 2017, Evaluation of *In Vitro* Bioactivity of 45S5 Bioactive Glass/Poly Lactic Acid Scaffolds Produced by 3D Printing. *Int J Compos Mater*, 7:144–9.
https://doi.org/10.5923/j.cmaterials.20170705.03

33. Aráoz B, Karakaya E, Wusener AG, *et al*., 2021, 3D Printed Poly(Hydroxybutyrate-co-hydroxyvalerate) 45S5 Bioactive Glass Composite Resorbable Scaffolds Suitable for Bone Regeneration. *J Mater Res*, 36:4000–12.
https://doi.org/10.1557/s43578-021-00272-9

34. Chartrain NA, Williams CB, Whittington AR, 2018, A Review on Fabricating Tissue Scaffolds Using Vat Photopolymerization. *Acta Biomater*, 74:90–111.
https://doi.org/10.1016/j.actbio.2018.05.010

35. Goswami A, Ankit K, Balashanmugam N, Umarji AM, *et al*., 2014, Optimization of Rheological Properties of Photopolymerizable Alumina Suspensions for Ceramic Microstereolithography. *Ceram Int*, 40:3655–65.
https://doi.org/10.1016/j.ceramint.2013.09.059

36. Hinczewski C, Corbel S, Chartier T, 1998, Ceramic Suspensions Suitable for Stereolithography. *J Eur Ceram Soc*, 18:583–90.
https://doi.org/10.1016/s0955-2219(97)00186-6

37. Eqtesadi S, Motealleh A, Miranda P, *et al*., 2014, Robocasting of 45S5 Bioactive Glass Scaffolds for Bone Tissue Engineering. *J Eur Ceram Soc*, 34:107–18.
https://doi.org/10.1016/j.jeurceramsoc.2013.08.003

38. Chen QZ, Thompson ID, Boccaccini AR, 2006, 45S5 Bioglass-derived Glass-ceramic Scaffolds for Bone Tissue Engineering. *Biomaterials*, 27:2414–25.
https://doi.org/10.1016/j.biomaterials.2005.11.025

39. Thavornyutikarn B, Tesavibul P, Sitthiseripratip K, *et al*., 2017, Porous 45S5 Bioglass(R)-based Scaffolds Using Stereolithography: Effect of Partial Pre-sintering on Structural and Mechanical Properties of Scaffolds. *Mater Sci Eng C Mater Biol Appl*, 75:1281–8.
https://doi.org/10.1016/j.msec.2017.03.001

40. Boccaccini AR, Chen Q, Lefebvre L, *et al*., 2007, Sintering, Crystallisation and Biodegradation Behaviour of Bioglass-derived Glass-ceramics. *Faraday Discuss*, 136:27–44; discussion 107–23.
https://doi.org/10.1039/b616539g

41. Woodard JR, Hilldore AJ, Lan SK, *et al*., 2007, The Mechanical Properties and Osteoconductivity of Hydroxyapatite Bone Scaffolds with Multi-scale Porosity. *Biomaterials*, 28:45–54.
https://doi.org/10.1016/j.biomaterials.2006.08.021

42. Fu Z, Zhuang Y, Cui J, *et al*., 2022, Development and

Challenges of Cells- and Materials-based Tooth Regeneration. *Eng Regen*, 3:163–81. https://doi.org/10.1016/j.engreg.2022.04.003

43. Wei H, Cui J, Lin K, *et al*., 2022, Recent Advances in Smart Stimuli-responsive Biomaterials for Bone Therapeutics and Regeneration. *Bone Res*, 10:17. https://doi.org/10.1038/s41413-021-00180-y
44. Bigham, A, Foroughi, F, Rezvani G, *et al*., 2020, The Journey of Multifunctional Bone Scaffolds Fabricated from Traditional toward Modern Techniques. *Biodes Manuf*, 3:281–306. https://doi.org/10.1007/s42242-020-00094-4
45. Zhang B, Pei X, Song P, *et al*., 2018, Porous Bioceramics Produced by Inkjet 3D Printing: Effect of Printing Ink Formulation on the Ceramic Macro and Micro Porous Architectures Control. *Compos Part B Eng*, 155:112–21. https://doi.org/10.1016/j.compositesb.2018.08.047

Publisher's note